Magnetic circular dichroism of terahertz modes and selection rules of Raman-active optical phonons in the polar altermagnet candidate $Mn_2Mo_3O_8$

F. Schilberth,[1] K. Vasin,[1,2] M. Knauft,[3] M. Kondákor,[4,5] M. Vuckovic,[1] N. Herrmann,[1] K. Penc,[5] M. Minola,[3] B. Keimer,[3] V. A. Martinez,[6] K. Panda,[6] A. A. Sirenko,[6] L. Prodan,[1] V. Tsurkan,[1,7] A. A. Tsirlin,[8] I. Kézsmárki,[1] and J. Deisenhofer[1]

[1]*Experimental Physics V, Center for Electronic Correlations and Magnetism, Institute for Physics, University of Augsburg, D-86159 Augsburg, Germany*

[2]*Institute for Physics, Kazan (Volga region) Federal University, 420008 Kazan, Russia*

[3]*Max Planck Institute for Solid State Research, Heisenbergstrasse 1, 70569 Stuttgart, Germany*

[4]*Department of Theoretical Physics, Institute of Physics, Budapest University of Technology and Economics, Műegyetem rkp. 3., H-1111 Budapest, Hungary*

[5]*Institute for Solid State Physics and Optics, HUN-REN Wigner Research Centre for Physics, H-1525 Budapest, P.O.B. 49, Hungary*

[6]*Department of Physics, New Jersey Institute of Technology, Newark, New Jersey 07102, USA*

[7]*Institute of Applied Physics, Moldova State University, str. Academiei 5, MD2028 Chisinau, Republic of Moldova*

[8]*Felix Bloch Institute for Solid-State Physics, Leipzig University, 04103 Leipzig, Germany*

(Received 1 August 2026; revised 22 September 2026; accepted 21 October 2026; published 17 November 2026)

We investigated the magnetic and vibrational excitations in the collinear altermagnet candidate $Mn_2Mo_3O_8$ by temperature-dependent Raman scattering and magneto-optical THz time-domain transmission spectroscopy. By comparison to *ab initio* calculations accurately capturing the eigenfrequencies of the vibrational eigenmodes, we identify all optical phonons, including the lowest-lying Raman modes of A_1 and E_2 type, which had remained elusive in a previous Raman study. Moreover, we compare the selection rules for optically active phonons in the paramagnetic and the magnetically ordered phases of $Mn_2Mo_3O_8$ and analyze the Raman selection rules with respect to pseudoangular momentum conservation. No splitting of the degenerate paramagnetic E_2 optical phonons into circularly polarized modes could be resolved below T_N, indicating negligible morphic effects of optical phonons upon magnetic ordering. In contrast, we observe strong magnetic circular dichroism at a broad THz excitation band, emerging in the magnetically ordered state. This band, potentially originating from two-magnon excitations, is only electric-dipole active and features a field-dependent two-component fine structure. Its magnetic circular dichroism vanishes above the spin-flop transition at 4 T.

DOI: 10.1103/sqws-q32r

I. INTRODUCTION

The polar molybdenum oxides $A_2Mo_3O_8$ (A = Mn, Fe, Co) exhibit collinear magnetic ground states, which can be changed by external magnetic fields or doping [1–10]. In the paramagnetic regime, these materials exhibit the nonsymmorphic polar hexagonal space group $P6_3mc$ (#186) with an intrinsic polarization along the c axis. The structural unit cell is shown in Fig. 1. The A^{2+} ions are responsible for magnetism, with half of them occupying the corner-sharing tetrahedral (A) and the other half the octahedral (B) sites. The Mo ions build nonmagnetic trimers [2,11,12].

As shown in Fig. 1(a), $Co_2Mo_3O_8$ and $Fe_2Mo_3O_8$ exhibit collinear AFM order along the c axis below $T_N = 39$ K [4,6–8,10] and $T_N = 60$ K [1,2], respectively. The magnetic structure of $Mn_2Mo_3O_8$ below $T_N = 40$ K corresponds to a ferrimagneticlike configuration with two ferromagnetic sublattices, one residing on the tetrahedral A-site, the other on the octahedral B-sites [see Fig. 1(b)] [13,14]. The temperature dependence of the magnetization in $Mn_2Mo_3O_8$ is shown in Fig. 2(a). The magnetization increases below $T_N = 40$ K, which had been attributed to a slightly canted spin state and different temperature dependences of the sublattice magnetization on A and B sites [13,14]. Towards lowest temperatures, these two sublattices completely compensate each other leading to a state with magnetization $\mathbf{M} \to 0$ for $T \to 0$ [15]. The magnetization as a function of magnetic field, shown in Fig. 2(b) at 5 K, identifies the onset of the spin-flop transition at about 4 T and exhibits a small hysteresis in low fields, which indicates the formation of ferrimagnetic domains in the magnetically ordered state [see inset of Fig. 2(b)]. These domains are aligned in fields exceeding 1 T at 5 K in agreement with previous reports [13].

The magnetic symmetries of these materials allow the observation of very interesting magneto-optical and magnetoelectric effects: For $Fe_2Mo_3O_8$, low-lying chiral phonons and magnon-polariton excitations in the THz frequency range have been reported [16–19], which exhibit nonreciprocal

Published by the American Physical Society under the terms of the Creative Commons Attribution 4.0 International license. Further distribution of this work must maintain attribution to the author(s) and the published article's title, journal citation, and DOI.

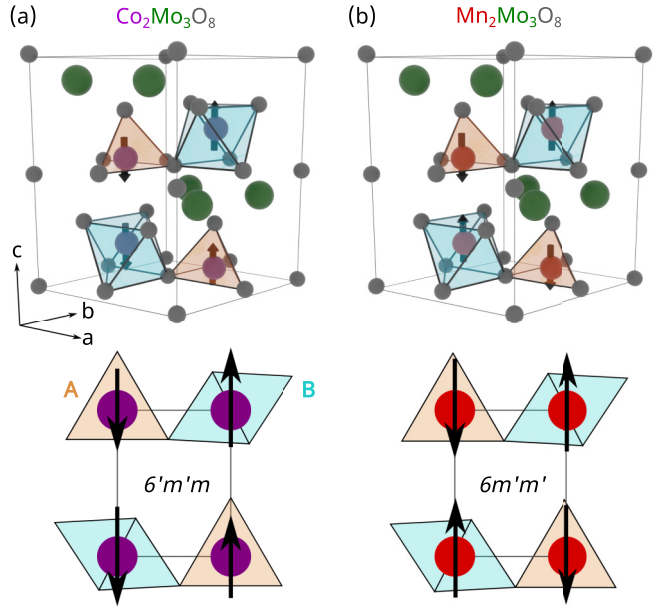


FIG. 1. Comparison of the different magnetic structures of (a) $Co_2Mo_3O_8/Fe_2Mo_3O_8$ and (b) $Mn_2Mo_3O_8$. While for $Co_2Mo_3O_8/Fe_2Mo_3O_8$ the compensated antiferromagnetic state comprises four magnetic sublattices within the magnetic point group $6'm'm$, $Mn_2Mo_3O_8$ is described by two magnetic sublattices within the magnetic point group $6m'm'$, which allows for ferrimagnetism.

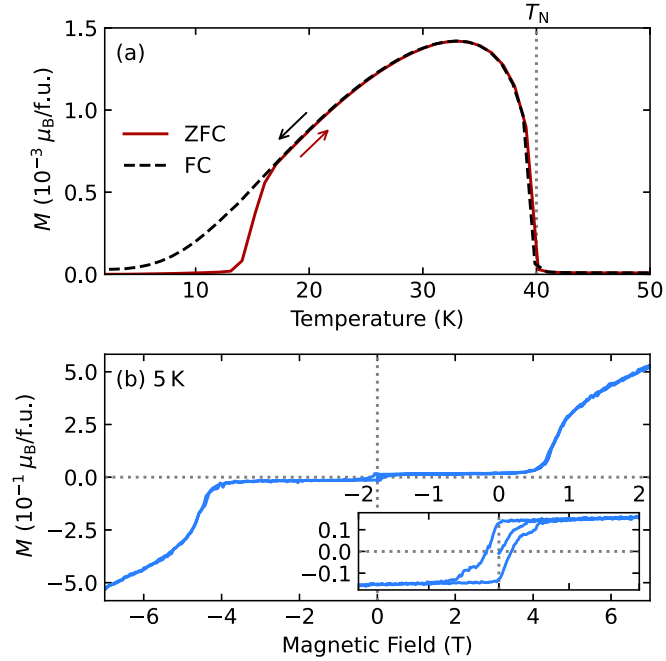


FIG. 2. (a) Magnetization of $Mn_2Mo_3O_8$ as a function of temperature measured upon heating after zero-field cooling (ZFC) and upon cooling in field (FC), both in a field of $H = 100$ Oe along the c axis. (b) Magnetization as a function of magnetic field along the c axis. The inset enlarges the hysteresis at low fields.

directional dichroism [7,19]. $Mn_2Mo_3O_8$ was shown to exhibit a linear magnetoelectric effect [3].

Recently, the three compensated collinear magnets $Fe_2Mo_3O_8$, $Co_2Mo_3O_8$, and $Mn_2Mo_3O_8$ have been discussed as altermagnet candidates [20–22]. In particular, within the broader classification based on compensated spins in the nonrelativistic limit and broken PT symmetry, the magnetic point group $6m'm'$ of $Mn_2Mo_3O_8$ has been classified as M-type altermagnetic [22]. Such compensated magnets can exhibit nonrelativistic spin splitting of electronic or magnonic bands at generic wave vectors in the Brillouin zone [23,24]. In a detailed study of optical phonons in the paramagnetic and magnetically ordered state of $Co_2Mo_3O_8$, the selection rules imposed by magnetic point groups and the proposed spin group approach for altermagnets were compared for infrared (IR)- and Raman-active phonons [25]. As a result, $Co_2Mo_3O_8$ proved to be a prominent realization of changes in the phonon sector due to magnetic order as described by Anastassakis and Burstein [26] using magnetic point groups. More generally, the change of phonon selection rules due to magnetic ordering or the application of external fields such as electric, magnetic, or strain fields have been described as *morphic effects* by Anastassasakis and Burstein in a series of pioneering papers in the 1970s [26–30], where the term morphic is related to the symmetry-adapted shape of the effective-charge tensor of the material in the presence of external fields or magnetic order. In contrast, the spin group approach for ideal altermagnets with $\mathbf{q} = 0$ antiferromagnetic order predicts, that there should be no changes with respect to the selection rules of optical phonons at the Γ point upon magnetic ordering [25].

Here, we follow a similar route for $Mn_2Mo_3O_8$, where the magnetic point group symmetry of the collinear magnetic state imposes a splitting of the doubly degenerate E-type phonons into conjugate left- and right-handed circularly polarized modes. Additionally, the previously silent modes become Raman- and infrared (IR) active below T_N. In order to reveal possible morphic effects, we investigated $Mn_2Mo_3O_8$ single crystals using THz-time domain and Raman spectroscopy and compared the observed modes to the eigenfrequencies obtained via *ab initio* calculations. The optical phonons of $Mn_2Mo_3O_8$ had been investigated by IR-reflectivity and Raman scattering across the magnetic ordering transition previously, without taking into account symmetry changes governed by magnetic ordering [31]. We additionally performed circularly polarized Raman measurements in the magnetically ordered state of $Mn_2Mo_3O_8$ and investigated the low-frequency IR-active excitations using THz-time domain spectroscopy in magnetic fields and circularly polarized THz radiation.

Compared to the previous studies, we elaborate on the selection rules of optical Raman modes for circular polarizations. The observed modes do not change upon entering into the magnetically ordered regime, i.e., we could not detect any changes in the phonon sector imposed by the symmetry lowering due to magnetic order, suggesting the suitability of the spin-group treatment for $Mn_2Mo_3O_8$. In addition, we find that the broad electric dipole active THz absorption consists of two components that exhibit magnetic circular dichroism. This effect disappears upon entering the spin-flop phase in fields above 4 T.

II. EXPERIMENTAL AND COMPUTATIONAL DETAILS

Transmission measurements were performed on a thin *ab* plane single crystal. By using a Bruker Fourier-transform IR-spectrometer Vertex80 equipped with a He-flow cryostat, the midinfrared (MIR) and near-infrared (NIR) frequency range from 1000 to 13 000 cm^{-1} and a temperature range from 5 to 300 K could be covered. THz time-domain spectroscopy measurements with linearly polarized light were performed in the temperature range 5–300 K on the same crystal using a TOPTICA TeraFlash pro THz system and a He-flow cryostat in transmission geometry at the University of Augsburg.

Circularly polarized magnetic-field-dependent time-domain THz transmission spectroscopy was performed at the National Synchrotron Light Source II at Brookhaven National Laboratory using a Toptica TeraFlash Pro spectrometer in magnetic fields ranging from −7 to 7 T. The magnetic field was applied in the Faraday geometry, perpendicular to the *ab* plane of the sample and parallel to the propagation direction of the THz beam ($\mathbf{k} \parallel \mathbf{B}$). Measurements were carried out at 5 K using a He-flow cryostat. Circular polarization was generated from broadband wire-grid linear polarizers in combination with achromatic optical retarders constructed from undoped Si prisms. With regard to the experimental details on the retarders and their function described in Ref. [32], we used an improved design of the retarders based on Si prisms and uncoated gold mirrors, which allowed us to eliminate the dispersion in the retardation parameters. With a retardation of 84.5°, these devices transform linearly polarized light almost perfectly into circularly polarized states $\mathbf{e}_+ = 1/\sqrt{2}(\mathbf{e}_x + i\mathbf{e}_y)$ and $\mathbf{e}_- = 1/\sqrt{2}(\mathbf{e}_x - i\mathbf{e}_y)$ with spin angular momenta $S_z = -\hbar$ and $S_z = +\hbar$ pointing along their propagation direction $\mathbf{k}$, yielding corresponding helicities $\sigma_\pm = \mathbf{k} \cdot \mathbf{S}/|\mathbf{k}| = \mp\hbar$, respectively. We observed no noticeable leakage between the two polarization channels. In order to define the nomenclature of left-handed and right-handed circularly polarized light, we chose the view of an observer looking in the direction of light propagation and call $\mathbf{e}_+$ as right-circularly polarized and $\mathbf{e}_-$ left-circularly polarized light [33,34].

Confocal Raman scattering experiments were performed using a LabRam HR800 spectrometer with an excitation wavelength of 633 nm from a HeNe-laser in backscattering geometry. For spectral analysis, a grating with 1800 grooves per mm was used. Both linearly or circularly polarized light was used to distinguish modes of different irreducible representations. The sample was fixed on a holder using silver paint and placed inside a He-flow cryostat. The indicated temperatures were measured at the holder position. During the experiment, the laser power was kept below 0.45 mW.

Density-functional-theory (DFT) band-structure calculations were performed in the `VASP` code [35,36] using the Perdew-Burke-Ernzerhof version of the exchange-correlation potential [37] and the experimental lattice parameters at 1.5 K: $a = 5.7943$ Å, $c = 10.2638$ Å. Phonon frequencies at the Γ-point were obtained by the finite-displacement method. Electronic correlations in the Mn $3d$ shell were taken into account on the mean-field level using the DFT + U procedure with the on-site Coulomb repulsion parameter $U_d = 5$ eV and Hund's coupling $J_d = 1$ eV [10]. The reported collinear low-temperature compensated ferrimagnetic configuration [14] was used.

III. SYMMETRY ANALYSIS AND SELECTION RULES FOR OPTICAL PHONONS

A. Irreducible representations and corepresentations

Phonon selection rules in nonmagnetic crystals are generally determined by the irreducible representations Γ of the crystallographic point group. In magnetic crystals, time reversal must also be taken into account. Unlike unitary spatial operations, time reversal is antiunitary, requiring the use of corepresentation theory. In the paramagnetic phase, the absence of static magnetic order makes the equilibrium state invariant under time reversal, and the relevant symmetry is therefore a gray magnetic group. For lattice vibrations and their conventional infrared and Raman selection rules, however, the resulting classification is equivalent to that of the underlying crystallographic point group. Once long-range magnetic order develops, the ordered moments define preferred directions in spin space. When spin and lattice degrees of freedom are coupled, symmetry operations must preserve the magnetic structure either directly or in combination with time reversal. This leads to magnetic space and point groups [38]. Within magnetic group theory, their irreducible corepresentations, denoted by $D\Gamma$, determine the optical-phonon selection rules in the magnetically ordered phase [25,26,38,39].

For paramagnetic $Mn_2Mo_3O_8$, whose crystallographic point group is $\mathbf{G} = 6mm$ and whose primitive unit cell contains two formula units, the 78 normal modes at the zone center decompose into irreducible representations as

$$\begin{aligned}\Gamma = {} & 9A_1(z; x^2+y^2, z^2) + 12E_1(x, y; xz, yz) && \text{(IR + Raman)}\\ & + 13E_2(x^2-y^2, xy) && \text{(Raman)}\\ & + A_1 + E_1 && \text{(acoustic)}\\ & + 3A_2 + 10B_1 + 3B_2 && \text{(silent),}\end{aligned} \quad (1)$$

where the corresponding symmetry-adapted basis functions are given in parentheses.

The nine optical A_1 modes can therefore be identified by direct IR transmission or reflectivity measurements with $\mathbf{E}^\omega \parallel c$, or by Raman scattering in the $x(zz)\bar{x}$ and $y(zz)\bar{y}$ configurations, using Porto notation [40,41], which is read from left to right starting with the propagation direction of the incoming light, then—in parentheses—the polarization state of the incoming light followed by the polarization state of the scattered light, and finally the propagation direction of the detected scattered light. Similarly, the 12 optical E_1 modes can be observed by IR transmission or reflectivity with $\mathbf{E}^\omega \parallel a$, i.e., with the electric field polarized in the hexagonal basal plane, or by Raman scattering in the $y(xz)\bar{y}$ and $x(yz)\bar{x}$ configurations. The remaining 13 E_2 modes are Raman active and can be observed in the $z(xy)\bar{z}$ configuration. These polarization configurations have previously been investigated for $Mn_2Mo_3O_8$ and the isostructural compounds $Co_2Mo_3O_8$ and $Fe_2Mo_3O_8$ using linearly polarized light, and the paramagnetic state selection rules were confirmed for many of the modes [25,31,42]. Raman measurements in the $z(xx)\bar{z}$

configuration provide an additional check because both A_1 and E_2 modes are symmetry-allowed in this channel. The intensities of the A_1 modes, however, need not to be the same as in the $x(zz)\bar{x}$ configuration because the two geometries probe different Raman tensor elements.

Below $T_N = 40$ K, long-range magnetic order develops together with a spontaneous magnetization, as shown in Fig. 2(a). Magnetic moments canted away from the c axis have been reported in the intermediate-temperature ordered phase of $Mn_2Mo_3O_8$ [14], whereas a collinear magnetic structure with vanishing net magnetization is established at the lowest temperatures [15]. This low-temperature collinear state is described by the magnetic space group $P6_3m'c'$ and the corresponding magnetic point group $6m'm'$ [14,43]. As in $Co_2Mo_3O_8$ and $Fe_2Mo_3O_8$, the magnetic ordering does not enlarge the primitive unit cell. Consequently, the number of normal modes remains 78.

To determine the phonon corepresentations of the magnetic point group, we follow the procedure of Anastassakis and Burstein [26]. For $Mn_2Mo_3O_8$ with magnetic point group $\mathbf{M} = 6m'm'$, the zone-center vibrational corepresentation decomposes into irreducible corepresentations as (see Tables VII and VIII in Appendix B)

$$\begin{aligned} D\Gamma = {} & 12DA(z; x^2+y^2, z^2) && \text{(IR+Raman)} \\ & + 12(D^1E_1 + D^2E_1)(x, y; xz, yz) && \text{(IR+Raman)} \\ & + 13(D^1E_2 + D^2E_2)(x^2-y^2; xy) && \text{(Raman)} \\ & + DA_1 + D^1E_1 + D^2E_1 && \text{(acoustic)} \\ & + 13DB && \text{(silent).} \end{aligned} \tag{2}$$

The corresponding symmetry-adapted linear and quadratic basis functions are again given in parentheses. Here we follow the convention that E_1 representations are odd and E_2 are even under the twofold rotation C_2 (see Table VII in Appendix B).

The magnetic group analysis predicts several morphic effects in $Mn_2Mo_3O_8$. In particular, the formerly silent A_2 modes may become optically active in the same polarization configurations as the A_1 modes. This occurs because both A_1 and A_2 reduce to the same irreducible representation A of the unitary halving subgroup $\mathbf{H} = 6$ and therefore belong to the same corepresentation DA of $\mathbf{M} = 6m'm'$.

Furthermore, the two-dimensional irreducible representations of $6mm$ decompose into one-dimensional complex-conjugate representations of $\mathbf{H} = 6$ according to

$$E_1 \to {}^1E_1 + {}^2E_1 \quad \text{and} \quad E_2 \to {}^1E_2 + {}^2E_2. \tag{3}$$

They form the corresponding corepresentations in $\mathbf{M} = 6m'm'$. As can be seen from Table VII, the ${}^1E_1$ (${}^1E_2$) and ${}^2E_1$ (${}^2E_2$) representations are complex conjugates and describe circularly polarized modes (this also holds for the corepresentations). Hence, each E_i ($i = 1, 2$) doublet of the paramagnetic state splits into left (D^1E_i) and right (D^2E_i) circularly polarized modes. A magnetic field applied along the sixfold axis does not further reduce the magnetic point group symmetry.

B. The spin group of $Mn_2Mo_3O_8$

We next discuss the spin group symmetry of $Mn_2Mo_3O_8$ and assess whether its low-temperature magnetic state exhibits altermagnetic characteristics. The tetrahedral and octahedral Mn sublattices are crystallographically inequivalent and host oppositely oriented magnetic moments that become nearly compensated at low temperatures. Moreover, the magnetic coupling parameters associated with the two sublattices in an effective description have been reported to be nearly identical [14].

As no symmetry operation connects the two magnetic sublattices, their compensation is not symmetry enforced. The low-temperature state may therefore be described as a compensated ferrimagnet, which does not belong to the class of rotation-related altermagnets. In the broader classification attempts of Refs. [20] and [22], however, the compensated nonrelativistic state with magnetic point group $6m'm'$ of $Mn_2Mo_3O_8$ is classified as an M-type altermagnet. For both classifications, the absence of symmetry-enforced degenerate magnon or electronic states allows nonrelativistic spin splitting at generic wave vectors. We therefore describe $Mn_2Mo_3O_8$ as an "altermagnet candidate" in this broader context.

To identify the spin symmetry underlying the collinear magnetic state, we adopt the spin group classification of Ref. [44]. In the nonrelativistic limit, the spin point group of a collinear magnet can be constructed as the direct product of its collinear spin-only group $\mathbf{b}^\infty$ and the corresponding magnetic point group. For $Mn_2Mo_3O_8$, this construction gives

$$6m'm' \times \mathbf{b}^\infty = {}^16^{\bar{1}}m^{\bar{1}}m, \tag{4}$$

which has Litvin index 399. This spin point group differs from that of $Co_2Mo_3O_8$ and $Fe_2Mo_3O_8$, ${}^16^{\bar{1}}m^1m$ (Litvin index 396). The difference originates from their distinct magnetic point groups, $6m'm'$ and $6'm'm$, respectively: The spin-flipping operations are combined with different real-space crystallographic operations in order to preserve the corresponding magnetic structures. As shown in Ref. [25], a corepresentation analysis based on the spin group recovers, in the nonrelativistic limit, the optical-phonon selection rules of the crystallographic point group $6mm$.

C. Conservation of pseudoangular momentum - Raman selection rules for phonons

In addition to energy and crystal-momentum conservation, pseudo-angular-momentum (PAM) conservation can further constrain the selection rules for first-order phonon Raman scattering. Tatsumi *et al.* derived the corresponding PAM-transfer rule for a phonon mode ν invariant under an N_ν-fold rotation of the crystal point group [45]. Defining the photon helicity change as $\Delta\sigma = \sigma_{\text{out}} - \sigma_{\text{in}}$, the conservation law takes the form

$$\Delta\sigma = -m_\nu^{\text{ph}} + N_\nu p, \quad p \in \mathbb{Z}, \tag{5}$$

where σ_{in} and σ_{out} are the helicities of the incoming and outgoing photons, respectively, in units of $\hbar$. Here, m_ν^{ph} denotes the PAM quantum number of the phonon mode. The term $N_\nu p$ expresses the conservation of PAM modulo the N_ν-fold rotational symmetry and represents the possible transfer of an integer multiple of $N_\nu\hbar$ to the lattice. The value of m_ν^{ph} is determined by the transformation of the phonon displacement eigenvector under the relevant rotation. For a nondegenerate

TABLE I. Selection rules for first-order Raman scattering of phonons arising from PAM conservation for the point groups $\mathbf{G} = 6mm$, $\mathbf{H} = 6$, and $\mathbf{M} = 6m'm'$ in $Mn_2Mo_3O_8$. The notation ✓ and × indicates whether a mode is allowed or forbidden by PAM and in the corresponding Raman configuration, where the PAM selection rules (columns for $\Delta\sigma$) have to be considered in addition to the symmetry adapted functions given in Eqs. (1) and (2). The selection rules including PAM for first-order Raman processes derived using Eq. (7) are given in given in the last 6 columns for the different Raman channels denoted in Porto notation.

						Helicity change $\Delta\sigma$			Raman configuration $z(\mathbf{e_{in}}\mathbf{e_{sc}})\bar{z}$					
$\mathbf{G} = 6mm$		dim	func.	N_ν	m_ν^{ph}	-2	0	2	(xx)	(xy)	$(\sigma_+\sigma_+)$	$(\sigma_-\sigma_-)$	$(\sigma_+\sigma_-)$	$(\sigma_-\sigma_+)$
	A_1	1	$z; x^2+y^2, z^2$	6	0	×	✓	×	✓	×	✓	✓	×	×
	A_2	1	–	6	0	×	✓	×	×	×	×	×	×	×
	B_1	1	–	3	0	×	✓	×	×	×	×	×	×	×
	B_2	1	–	3	0	×	✓	×	×	×	×	×	×	×
	E_1	2	$x, y; xz, yz$	1	$0, (-1, +1)$	✓	✓	✓	×	×	×	×	×	×
	E_2	2	x^2-y^2, xy	2	$0, (-1, +1)$	✓	✓	✓	✓	✓	×	×	✓	✓
$\mathbf{H} = 6$	$\mathbf{M} = 6m'm'$													
A	DA	1	$z; x^2+y^2, z^2$	6	0	×	✓	×	✓	×	✓	✓	×	×
B	DB	1	–	3	0	×	✓	×	×	×	×	×	×	×
${}^1E_1$	$D\,{}^1E_1$	1	$x - \mathrm{i}y, xz - \mathrm{i}yz$	1	0	✓	✓	✓	×	×	×	×	×	×
					-1	✓	✓	✓	×	×	×	×	×	×
${}^2E_1$	$D\,{}^2E_1$	1	$x + \mathrm{i}y, xz + \mathrm{i}yz$	1	0	✓	✓	✓	×	×	×	×	×	×
					$+1$	✓	✓	✓	×	×	×	×	×	×
${}^1E_2$	$D\,{}^1E_2$	1	$(x^2-y^2) + 2\mathrm{i}xy$	2	0	✓	✓	✓	✓	✓	×	×	×	✓
					-1	×	×	×	×	×	×	×	×	×
${}^2E_2$	$D\,{}^2E_2$	1	$(x^2-y^2) - 2\mathrm{i}xy$	2	0	✓	✓	✓	✓	✓	×	×	✓	×
					$+1$	×	×	×	×	×	×	×	×	×

zone-center phonon transforming according to a real irreducible representation, the displacement eigenvector can be chosen real. Such a mode carries no angular momentum and has $m_\nu^{\mathrm{ph}} = 0$ within the present convention. This argument does not, however, apply to modes belonging to complex one-dimensional representations.

In the following, we derive the PAM selection rules for the irreducible representations and corepresentations relevant to $Mn_2Mo_3O_8$. In particular, we extend the analysis to complex one-dimensional representations, such as the D^1E_2 and D^2E_2 corepresentations, which were not explicitly considered in Ref. [45]. Complex-conjugate pairs of one-dimensional irreducible representations occur in the crystallographic point groups 4, $\bar{4}$, $4/m$, 3, $\bar{3}$, 6, $\bar{6}$, $6/m$, 23, and $m\bar{3}$, and in magnetic point groups constructed from them [38].

To characterize the circular motion associated with a phonon mode, we follow the formulation of Zhang and Niu [46]. For a normalized phonon polarization vector $\boldsymbol{\epsilon}_{\nu,n}$, the component of the PAM along the crystallographic z axis, coinciding with the light propagation direction in our experiment, carried by mode ν is

$$\hbar m_\nu^{\mathrm{ph}} = \hbar \sum_n \boldsymbol{\epsilon}_{\nu,n}^\dagger \cdot \begin{pmatrix} 0 & -\mathrm{i} & 0 \\ \mathrm{i} & 0 & 0 \\ 0 & 0 & 0 \end{pmatrix} \cdot \boldsymbol{\epsilon}_{\nu,n}, \tag{6}$$

where n labels the atoms in the primitive unit cell. A nonzero value of m_ν^{ph} indicates a chiral phonon whose atomic displacements exhibit a net circular polarization about the z axis. By analyzing the phonon eigenvectors and their contributions from the different Wyckoff positions, one can identify the modes with nonzero angular momentum and assign them to the corresponding irreducible representations. The resulting PAM quantum numbers m_ν^{ph} are listed in Table I.

For $Mn_2Mo_3O_8$, our analysis shows that the finite PAM of the chiral phonon modes originates from the displacements of the atoms occupying the $2a$ and $2b$ Wyckoff positions, namely four Mn and four O atoms in the primitive unit cell. The site-symmetry groups of these positions contain a threefold rotation axis parallel to z, allowing circularly polarized displacement patterns about this axis.

In the paramagnetic phase, these modes belong to the two-dimensional irreducible representations E_1 and E_2, whose two components form time-reversal-related pairs with opposite PAM quantum numbers, $m_\nu^{\mathrm{ph}} = (-1, +1)$, as listed in Table I. In the magnetically ordered phase, the E_1 and E_2 representations decompose into the corepresentations D^1E_1, D^2E_1, D^1E_2, and D^2E_2. These corepresentations host modes of opposite circular polarization; symmetry does not enforce degeneracy. As follows from Eq. (6), a phonon polarization vector that can be chosen real has vanishing angular momentum, $m_\nu^z = 0$ [45,46]. In our phonon polarization vectors, the 6 Mo and 12 O atoms occupying the $6c$ Wyckoff positions do not contribute to the net PAM of these modes. This agrees with the fact that their site-symmetry groups, m in the paramagnetic phase and m' in the magnetically ordered phase, do not contain complex characters.

We make two additional assumptions in applying the PAM selection rules to $Mn_2Mo_3O_8$. First, we restrict the analysis to zone-center phonons within the harmonic approximation. At $\mathbf{k} = 0$, the translational part of a screw operation contributes no Bloch phase factor. The screw operation nevertheless permutes symmetry-related atomic sites within the unit cell and rotates their displacement vectors; both effects must be

included in its action on the full phonon eigenvector $\boldsymbol{\epsilon}_\nu$. Thus, at the zone center, the phonon PAM is determined by the phase acquired by the complete displacement pattern under the screw operation, including both the rotation of the displacement vectors and the permutation of the basis atoms. Because its fractional translation produces no additional phase at the zone center, the sixfold screw axis of $Mn_2Mo_3O_8$ is represented by its sixfold rotational counterpart in the point group classification.

Second, we assume that no proper rotation relevant to PAM conservation is combined with an antiunitary operation, as is the case for $Mn_2Mo_3O_8$. These conditions allow us to apply the approach of Tatsumi *et al.* [45]. In the magnetic point group $\mathbf{M} = 6m'm'$, all antiunitary operations are reflections (i.e., reflections and glide planes in the magnetic space group). Although these antiunitary operations impose additional constraints on the Raman tensors, as summarized in Table IX in Appendix B, they do not modify the PAM-conservation rule imposed by proper rotations.

The resulting selection rules for the different Raman configurations are summarized in Table I. They may be represented schematically by combining the conventional Raman-tensor selection rule with the PAM-conservation condition:

$$I_{R,\nu} \propto |\mathbf{e}_{\mathrm{Sc}}^{*} \cdot \hat{R}_\nu \cdot \mathbf{e}_{\mathrm{In}}|^2 \sum_{p\in\mathbb{Z}} \delta_{\Delta\sigma + m_\nu^{\mathrm{ph}} - N_\nu p,\,0}, \tag{7}$$

where $\mathbf{e}_{\mathrm{In}}$ and $\mathbf{e}_{\mathrm{Sc}}$ are the polarization vectors of the incoming and scattered light, respectively, and $\hat{R}_\nu$ is the Raman tensor of phonon mode ν [47]. The first factor gives the conventional polarization selection rule, whereas the Kronecker delta enforces PAM conservation modulo the N_ν-fold rotational symmetry. The symmetry-adapted Raman tensors for the crystallographic point group $6mm$ and the magnetic point group $6m'm'$ are given in Table IX in Appendix B. They determine the symmetry-allowed Raman channels associated with the basis functions listed in Table I. Combining these tensor constraints with PAM conservation yields the selection rules listed in the final six columns of Table I for the different Raman configurations expressed in Porto notation.

One can associate Eq. (7) with Eq. (2) in the work by Tatsumi and coworkers [45]. In a microscopic treatment, the effective Raman tensor $\hat{R}$ arises from electron-photon coupling, whereas PAM conservation applies to the complete scattering process including the electron-phonon interaction [45].

The main question is whether PAM conservation imposes additional selection rules beyond those obtained from the crystallographic Raman tensors. In an ideal collinear backscattering geometry, the circular components of the incoming and scattered photons correspond to a transferred angular momentum of 0 or $\pm 2\hbar$ along the scattering axis. Based on Eq. (7) and Table I, the only crystallographically Raman-active modes in $Mn_2Mo_3O_8$ for which this constraint may produce an additional exclusion are the paramagnetic E_2 and ordered D^1E_2 and D^2E_2 modes with $m_\nu^{\mathrm{ph}} = \pm 1$.

In the paramagnetic phase, the two components of each E_2 doublet are related by time reversal, leading to degeneracy. Consequently, one may take their real linear combinations with vanishing angular momentum $m_\nu^{\mathrm{ph}} = 0$, which can satisfy the PAM selection rule for a helicity change of ± 2 through a rotational umklapp process with $N_\nu = 2$, so theory allows the observation of the paramagnetic E_2 modes.

Within the magnetic point group description of the ordered phase, E_2 doublets decompose as $E_2 \rightarrow D^1E_2 + D^2E_2$, leading to nondegenerate phonon modes that may carry finite angular momentum. One may therefore expect changes in the Raman spectra in general, concerning the positions and the splitting of the paramagnetic peaks, and the selection rules by PAM conservation may become observable. However, these effects may be too weak to be resolvable in experiments. The absence of detectable morphic effects suggests weak coupling between the lattice vibrations and magnetic degrees of freedom and is therefore consistent with the applicability of a nonrelativistic spin-group description, although it does not explicitly establish or exclude nonrelativistic altermagnetic spin splitting. As we present in the next sections, we observe neither a resolvable splitting nor additional selection rules upon entering the magnetically ordered phase in $Mn_2Mo_3O_8$ in agreement with predictions using the spin group approach.

IV. EXPERIMENTAL RESULTS AND DISCUSSION

A. Raman scattering of optical phonons

Following the discussion of possible morphic effects and the correspondig selection rule given by Eqs. (1) and (2), we reinvestigated the temperature dependence of the Raman active E_2 modes across the magnetic ordering transition in the Raman channels $z(xx)\bar{z}$, $z(xy)\bar{z}$, $z(\sigma_+\sigma_-)\bar{z}$, and $z(\sigma_-\sigma_+)\bar{z}$. The corresponding spectra are shown in Fig. 3 and the eigenfrequencies obtained by fitting the spectra with Lorentzian line shapes are compared to the calculated eigenfrequencies in Table II. As we focused in our experiments on the low-frequency regime in order to observe the so-far evasive lowest-lying E_2 modes, we restricted the range to below 350 cm^{-1}. However, we additionally list the eigenfrequencies of all Raman modes reported previously for the configuration $z(xy)\bar{z}$ by Stanislavchuk *et al.* [31] to compare all observable eigenfrequencies with our calculations. A comparison of our calculations to the observed IR- and Raman active modes by Stanislavchuk in the Raman configuration channels $y(zz)\bar{y}$ and $y(xz)\bar{y}$ is provided in Table IV in Appendix A. An improved agreement between the experimental and calculated frequencies compared to Ref. [31] is due to the use of DFT + U in phonon calculations.

In Figs. 3(a) and 3(b) the Raman spectra for the configuration $z(xx)\bar{z}$ and $z(xy)\bar{z}$, respectively, are shown at 85 K in the paramagnetic state and 5 K in the magnetically ordered state. The temperatures were chosen to match the ones used in the previous Raman study by Stanislavchuk *et al.* [31]. All expected E_2 modes in this frequency range are observed in both configurations, including the lowest-lying $E_2(1)$ with an eigenfrequency of about 63.5 cm^{-1} at 5 K. Almost no shift in eigenfrequencies was observed between the two temperatures, indicating a weak coupling between the spin and lattice degrees of freedom in $Mn_2Mo_3O_8$. In $z(xx)\bar{z}$ configuration the A_1 modes are allowed in addition to the E_2 modes. Their calculated eigenfrequencies are given in Table IV in

TABLE II. Experimental Raman excitation frequencies in $Mn_2Mo_3O_8$ (in cm^{-1}) measured in $z(xy)\bar{z}$ and $z(xx)\bar{z}$ configuration, as well as $z(\sigma_+\sigma_-)\bar{z}$ and $z(\sigma_-\sigma_+)\bar{z}$ configuration in the paramagnetic phase at 85 K and in the magnetically ordered phase at 5 K. Mode assignment is made by comparison with calculated phonon eigenfrequencies obtained from *ab initio* calculations for the 13 expected $E_2(i)$ modes $i = 1, \ldots, 13$ and to the nine expected $A_1(j)$ modes $j = 1, \ldots, 9$ (see Table IV in Appendix A for all calculated eigenfrequencies). Assignment of the mode at 292 cm^{-1} in the last row as a longitudinal optical (LO) A_1 mode is tentative as discussed in the text.

this work						Ref. [31]		Mode
$z(xx)\bar{z}$		$z(xy)\bar{z}$		$z(\sigma_+\sigma_-)\bar{z}$, $z(\sigma_-\sigma_+)\bar{z}$		$z(xy)\bar{z}$		assignment
85 K	5 K	85 K	5 K	85 K	5 K	85 K	5 K	E_2(i) (calc.)
64.1	63.3	64.2	63.5	64.0	63.5	-	-	58
143	143	143	143	143	143	140	140	143
185	184	185	184	185	184	184	183	180
216	215	216	215	215	215	214	214	210
266	266	266	266	266	266	265	265	261
325	326	325	326	325	326	323	324	318
345	345	345	345	345	345	343	343	342
-	-	-	-	-	-	442	442	424
-	-	-	-	-	-	461	461	449
-	-	-	-	-	-	474	474	465
-	-	-	-	-	-	514	514	507
-	-	-	-	-	-	555	555	552
-	-	-	-	-	-	733	733	726
204	204	-	-	-	-	-	-	$A_1(1)$ (calc.) at 203
292	292	-	-	-	-	-	-	$A_1(2)$ (LO)

Appendix A. Only the lowest-lying $A_1(1)$ mode was observed in our experiment. The overall agreement of the observed and calculated eigenfrequencies is very good and all expected phonon modes could be identified. It is noteworthy to mention that the calculated eigenfrequencies for the A_1 and E_1 in Table IV in Appendix A are in good agreement with previously reported experimental values obtained by Raman scattering and IR reflectivity, too [31].

Moreover, an additional mode at 292 cm^{-1} is observed in the $z(xx)\bar{z}$ channel at both temperatures, which does not correspond to any of the calculated phonon eigenfrequencies. We attribute the origin of this mode tentatively to the longitudinal optical eigenfrequency of mode $A_1(2)$, based on the fact that several longitudinal A_1 modes have been identified in the isostructural materials $Co_2Mo_3O_8$ and $Fe_2Mo_3O_8$, too [25]. The occurrence of longitudinal modes in these materials has been discussed in terms of intrinsic resonant Raman scattering effects [25]. Resonant Raman effects can always occur, if the laser frequency is larger than the band gap of the material (see Martin and Falicov in Ref. [48]). This is also the case for $Mn_2Mo_3O_8$, where our transmission measurements in the MIR-/NIR frequency regime provide an estimate of about 0.84 eV (see Fig. 6 in Appendix C), which is clearly lower than the photon energy of the 633-nm laser (1.96 eV). Additional Raman modes reported by Stanislavchuk *et al.* [31] can also be tentatively assigned to such longitudinal and transverse A_1 modes (see Tables V and VI in Appendix A), confirming a similar pattern as in $Co_2Mo_3O_8$ and $Fe_2Mo_3O_8$.

In Figs. 3(c) and 3(d) we show Raman spectra taken at 85 and 5 K for the crossed circular-polarization channels $z(\sigma_+\sigma_-)\bar{z}$ and $z(\sigma_-\sigma_+)\bar{z}$ in order to compare with the derived selection rules in Table I. The mode $A_1(1)$ is allowed in $z(xx)\bar{z}$ both by symmetry of the Raman tensor and PAM conservation, for $z(\sigma_+\sigma_-)\bar{z}$ and $z(\sigma_-\sigma_+)\bar{z}$ actually both factors in Eq. (7) are zero and the A_1 and *DA* modes are forbidden in these configuration. With respect to the predicted selection rules for the $D\,^2E_2$ and $D\,^1E_2$ corepresentations, we find no evidence of changes upon entering into the magnetically ordered phase—all modes in the investigated frequency range are observed as in the channels $z(xx)\bar{z}$ and $z(xy)\bar{z}$. We could neither resolve the possible splitting nor observe any circular polarization dependence. This suggests that spin-lattice coupling in $Mn_2Mo_3O_8$ is rather weak and the splitting might be of the order of 10^{-3} as predicted by Sokolov using a Heisenberg Hamiltonian, where the spin-lattice coupling is mediated by the modulation of the exchange integral by lattice vibrations in first order perturbation theory [49]. As discussed above, the application of a magnetic field along the c axis is compatible with the magnetic point group $6m'm'$, but might increase the splitting of the $D\,^1E_1$, $D\,^2E_1$, $D\,^1E_2$, and $D\,^2E_2$ irreducible corepresentations as long as it does not change the collinear spin configuration and the magnetic point group, e.g., by the spin-flop transition in fields above 4 T [see Fig. 2(b)].

B. THz-time domain magnetospectroscopy

In Fig. 4(a) we show the temperature dependence of the absorption coefficient of $Mn_2Mo_3O_8$ across the magnetic ordering transition for light polarization configuration $E^\omega, H^\omega \perp c$, where a broad peak called TM emerges at around 60 cm^{-1} from a continuumlike background. The maximum of the TM mode at 4 K is at 58 cm^{-1} (1.74 THz). The peak was previously reported to be only electric-dipole

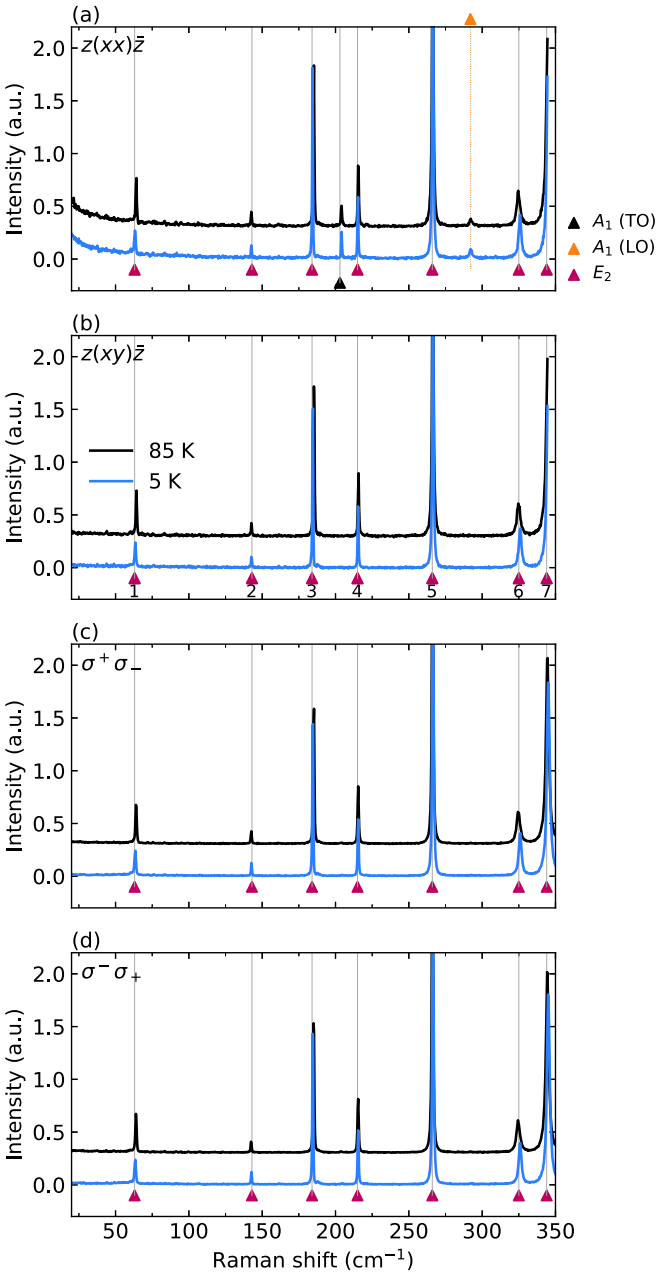


FIG. 3. Comparison of Raman spectra at 85 K (black) and 5 K (blue) in scattering configurations (a) $z(xx)\bar{z}$ allowing for the observation of E_2 and A_1 modes, (b) $z(xy)\bar{z}$ corresponding to the irreducible E_2 representations of the paramagnetic phase. The determined eigenfrequencies of phonon modes expected for each configuration in the paramagnetic phase are indicated by upward triangles at the bottom of the individual panels. Symbols at the top of the panels indicate modes different from expected modes of the paramagnetic phase as described in the text. (c) and (d) Comparison of Raman spectra in crossed circular polarization configurations $z(\sigma_+\sigma_-)\bar{z}$ and $z(\sigma_-\sigma_+)\bar{z}$ at 5 and 85 K.

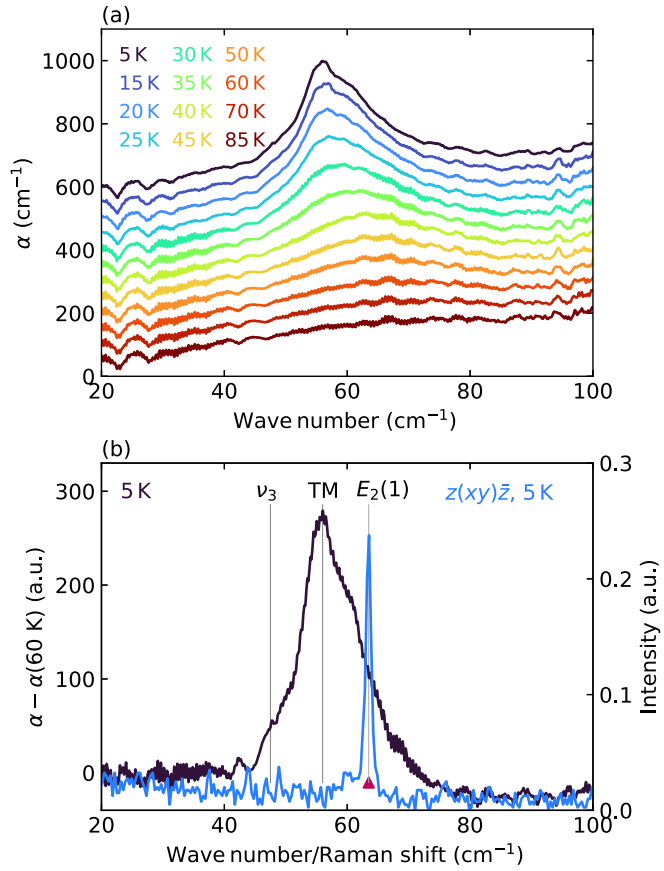


FIG. 4. (a) Temperature dependence of the absorption coefficient α in $Mn_2Mo_3O_8$ for light polarization configuration $E^\omega, H^\omega \perp c$ crossing into the magnetically ordered state at $T_N = 40$ K. (b) Comparison of the absorption difference $\Delta\alpha = \alpha(5\ \text{K}) - \alpha(60\ \text{K})$ (black)—revealing the excitations ν_3 and TM previously reported in [13]—and the lowest-lying $E_2(1)$ Raman mode (blue) in the magnetically ordered state at $T = 5$ K.

active for the polarization configuration $E^\omega \perp c$ [13], which our measurements confirm. The reported low-lying magnon modes ν_1 and ν_2 observed in zero magnetic field have eigenfrequencies of about 3.8 and 5 cm^{-1}, which is below our experimental low-frequency cutoff. The reported weak mode ν_3 at 47.8 cm^{-1} is also visible at the low-energy flank of the TM mode in Fig. 4(b). As all reported zero-field magnon excitations at the Γ-point are at lower energies in $Mn_2Mo_3O_8$ [13,14], the most likely mechanism to account for this broad electric-dipole active THz excitation band is a two-magnon process [13], where two magnons with opposite propagation vectors can be excited simultaneously by light with $q \approx 0$ [50–53]. Such processes have first been observed in the rutile antiferromagnets FeF_2 [54] and MnF_2 [55] and attributed to an exchange mechanism [50], without the need for spin-orbit coupling induced processes as it had been suggested previously [54]. Notably, no such broad excitation has been observed in THz spectra of $Co_2Mo_3O_8$ [7,25] and $Fe_2Mo_3O_8$ [19], where instead phonons are coupled to magnon excitations [17,18]. In Fig. 4(b) we compare the broad THz excitation at 5 K after subtraction of the spectrum at 60 K as a nonmagnetic background with the lowest-lying Raman mode $E_2(1)$ at 5 K. Although the eigenenergy of the Raman mode matches well with the high-energy flank of the THz excitation, its width is much narrower than the one of the THz excitation and we conclude that the THz excitation *TM* is not strongly influenced by spin-phonon coupling.

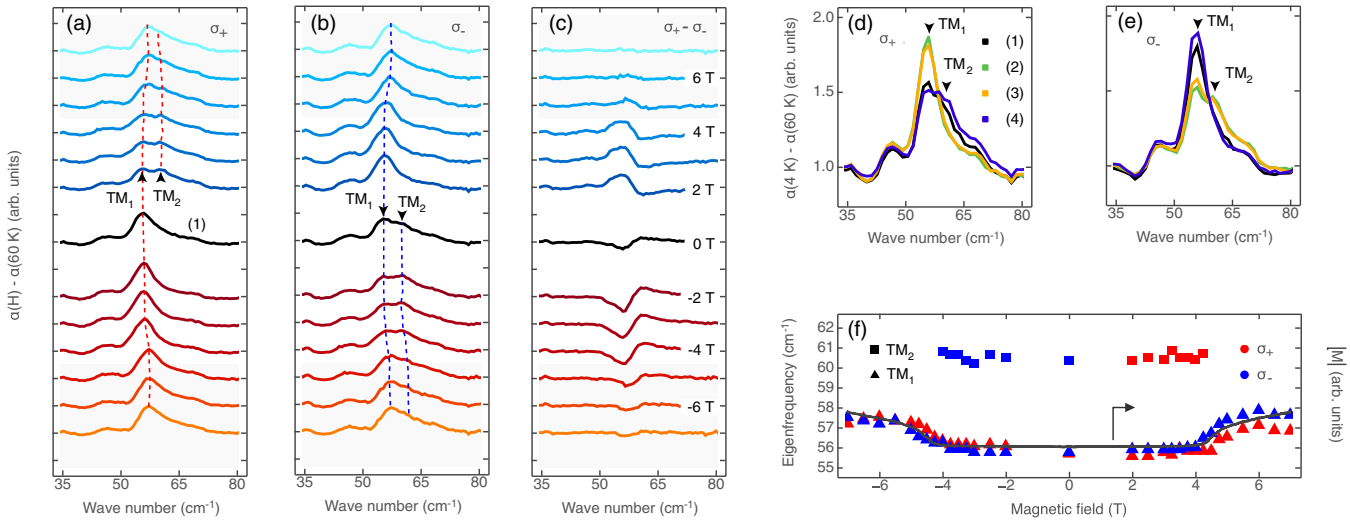


FIG. 5. Magnetic field dependence of absorption difference spectra for (a) right circularly polarized light (σ_+), (b) left circularly polarized light (σ_-), and (c) the difference of right and left circularly polarized spectra $\sigma_+ - \sigma_-$. (d) and (e) show the zero-field absorption spectra for σ_+ and σ_-, where (1) corresponds to the first zero-field cooled spectra, (2) to the spectrum taken after the sweep to +7 T, (3) to the one taken after heating to 60 K and zero-field cooling again down to 5 K, and (4) to the one taken after the sweep to −7 T. (f) Magnetic field dependence of the peak frequencies of TM_1 and TM_2 in comparison to the modulus of the magnetization shown in Fig. 2(b).

To further elucidate the origin of this THz excitation, we performed THz-time domain magnetospectroscopy using left and right circularly polarized light in transmission geometry and in fields up to ±7 T. The sample was first cooled to 5 K in zero field and at each field step from 0 to +7 T, transmission spectra with left and right circularly polarized light were measured. Note that in this more complex optical setup, the weak feature assigned as ν_3 in Fig. 4(b) was not resolved in the circularly polarized experiments. After the magnetic field was ramped down to zero, the sample was heated to 60 K and then cooled down to 5 K and transmission spectra were measured in fields from 0 to −7 T. The corresponding spectra for σ_+ and σ_- circularly polarized light are shown for all fields from −7 to 7 T in Figs. 5(a) and 5(b), respectively, after subtraction of the spectra at 60 K as a paramagnetic background. Zero-field spectra were taken before and after each field sweep and they are compared in Figs. 5(d) and 5(e). It is clear from this comparison that the zero-field absorption spectra using circularly polarized light depends on its history, which can be expected given the small magnetic hysteresis shown in Fig. 2(b). The spectra in zero-field exhibit a clear magnetic circular dichroism, i.e., a difference in the absorption using σ_+ and σ_- circularly polarized light. Either the spectrum is dominated by a single peak TM_1 at 57 cm^{-1} or the spectrum shows a two-peak structure consisting of TM_1 and the second contribution TM_2 with maxima at 56 and 62 cm^{-1}, respectively. Upon application of a magnetic field from 0 to about +4 T, it becomes clear that TM_1 appears to be dominant for σ_- circularly polarized light, while the second maximum indicating TM_2 seems to be visible only for σ_+ polarized light. This situation is reversed for negative fields from 0 to −4T. For fields exceeding ±4 T the system enters into the spin-flopped phase and only the low-frequency maximum remains discernible with a high-energy flank that might contain contributions of TM_2.

Notably, above the spin-flop transition the spectra exhibit a similar shape suggesting that both TM_1 and TM_2 are excited independently of the light polarization or field direction and the magnetic circular dichroism is much weaker. In order to highlight field-dependent changes in the spectra, which do not depend on the circular light polarization state, we plot the difference of the spectra taken with right and left circularly polarized light for each field in Fig. 5(c). These difference spectra reveal components, which are changing with the helicity of the THz light and should compensate all features unrelated to the polarization state. As expected, the magnetic circular dichroism of the spectra is only related to the frequency range of the TM_1 and TM_2 contributions and at ±7 T in the spin-flop phase the flat lines indicate that no MCD is present anymore. In Fig. 5(f) we show the peak frequencies of the TM_1 and TM_2 obtained by parametrizing the two contribution by Lorentzian line shapes. The onset of the spin-flop transition is clearly mirrored by a shift of TM_1 to higher frequency, which can be scaled with the modulus of the magnetization shown in Fig. 2(b). The maximum of TM_2 can not be determined unambiguously anymore in the spin-flop phase.

At present, it is unclear how the observed magnetic dichroism and the two-component nature of the THz absorption can be reconciled with the suggested two-magnon process underlying this excitation. We list the Brillouin-zone edge energies of the observed magnon dispersions measured by neutron scattering in Table III. While none of these doubled magnon energies corresponds directly to the maxima of TM_1 and TM_2 branches alone, the combinations of different magnon branches could provide energies in the range of the broad excitation continuum consisting of TM_1 and TM_2. Whether such two-magnon processes involving different magnon branches are optically allowed at all and could explain the observed magnetic circular dichroism of the absorption, requires,

TABLE III. Magnon energies at the Brillouin zone boundaries taken from Ref. [14].

Q (H,K,L)	Mode	Energy [meV]	Wave number [cm^{-1}]
Γ_2 (0,1,0)	M_1	1.9	15
	M_2	3.0	24
M (1/2,1,−1)	M_3	4.5	35
	M_4	6.2	50
K (2/3,2/3,−1)	M_5	5.4	44
	M_6	6.8	55

however, a detailed microscopic approach, which is beyond the scope of this paper.

V. CONCLUSION

In summary, we investigated the polar magnet $Mn_2Mo_3O_8$ by THz-time domain magnetospectroscopy and Raman scattering and performed a detailed analysis of the pseudoangular momentum conservation during the Raman process considering the crystallographic and magnetic point groups of the system. Moreover, we calculated the phonon eigenfrequencies for $Mn_2Mo_3O_8$ and find them in good agreement with the experimental ones reported both in this work and in a previous study [31], which also reported infrared-active modes. As such all expected phonon modes have now been identified. Our Raman measurements do not reveal any activation of previously silent modes or splittings and chiral features of phonon modes upon magnetic ordering, although such processes become allowed by the symmetry lowering due to magnetic order. We conclude therefore, that the optical phonons in $Mn_2Mo_3O_8$ follow the same selection rules both in the paramagnetic and magnetically ordered state and do not exhibit morphic effects due to magnetic order. Such a behavior is expected for magnets which can be described by spin groups with decoupled spatial and spin degrees of freedom [25]. In contrast to the sister compounds $Fe_2Mo_3O_8$ and $Co_2Mo_3O_8$, the half-filled d shell of the Mn^{2+} ions leads to comparatively weak relativistic effects in the phonon sector. Hence, $Mn_2Mo_3O_8$ is an interesting candidate for nonrelativistic spin-split electronic and magnonic bands, one of the characteristic reciprocal-space signatures associated with altermagnetism. Importantly, we observe that the electric-dipole active THz excitation band TM emerging in the magnetically ordered state shows large magnetic circular dichroism below the spin-flop transition. While the continuumlike line shape, the electric-dipole activity, and the energy scale with respect to reported magnon dispersions clearly point towards a two-magnon nature of this excitation, the observed magnetic circular dichroism remains to be reconciled with this scenario.

ACKNOWLEDGMENTS

This research was partly funded by the Deutsche Forschungsgemeinschaft (DFG, German Research Foundation)-TRR 360-492547816. TRR 360-492547816 and the Hungarian National Research, Development and Innovation Office (NKFIH) through OTKA Grant No. K 142652. THz magnetospectroscopy by K.P. and A.A.S. were supported by the U.S. Department of Energy (DOE) Grant No. DE-FG02-07ER46382. Experiments at the National Synchrotron Light Source II at Brookhaven National Laboratory were funded by the DOE No. DE-AC9806CH10886. The NSF MPS-ASCEND Award No. 2316535 supported experiments performed by V.A.M. The authors gratefully acknowledge the use of computing resources of the ALCC HPC cluster (Institute of Physics, University of Augsburg). V.T. acknowledges the support by the project ANCD (cod 011201 Moldova).

DATA AVAILABILITY

The Raman and THz spectra as well as the magnetization data are available on Zenodo [56].

APPENDIX A: CALCULATED PHONON EIGENFREQUENCIES FOR $Mn_2Mo_3O_8$ AND COMPARISON TO INFRARED AND RAMAN DATA

Here we will discuss all calculated eigenfrequencies for the normal modes as listed in Table IV with respect to the observed IR- and Raman-active modes as reported by Stanislavchuk *et al.* [31]. For the nine A_1 modes in Table V, a very good agreement between theory and experiment is observed with both the IR-active modes reported for $\mathbf{E}^{\omega} \parallel c$ and the Raman-active modes in the Raman configuration $y(zz)\bar{y}$. No signature of an additional activity of the A_2 modes as a part of the corepresentation DA in the magnetically ordered phase has been found in the spectra at 5 K. Notably, the lowest lying $A_1(1)$ mode was only observed in the IR channel and not in the $y(zz)\bar{y}$ Raman channel, while in our spectra in $z(xx)\bar{z}$ configuration the mode has been observed (see Fig. 3(a) and Table II). Instead, mode $A_1(4)$ was only detected in the Raman channel.

In addition, there is a mode observed only in the Raman channel at 668 cm^{-1} at both temperatures and a mode at 844 cm^{-1} appearing in both channels at both temperatures.

TABLE IV. Calculated phonon eigenfrequencies (in cm^{-1}) of the low-temperature magnetic phase ($T = 1.7$ K) in $Mn_2Mo_3O_8$. The calculations do not reveal a splitting of the E_1 and E_2 representations in the magnetically ordered state.

A_1/DA	A_2/DA	B_1/DB	B_2/DB	E_1/D^iE_1	E_2/D^iE_2
203	141	150	142	157	58
256	374	207	406	186	143
371	410	248	380	216	180
439		365		270	210
449		438		301	261
549		477		337	318
631		565		425	342
709		633		447	424
775		716		464	448
		810		505	465
				557	507
				721	552
					726

TABLE V. Experimental excitation frequencies (in cm^{-1}) in $Mn_2Mo_3O_8$ of IR-active modes for light polarization $\mathbf{E}^{\omega} \parallel c$ and Raman-active modes in the Raman configuration $y(zz)\bar{y}$ measured at 85 and 5 K as reported in [31] in comparison to the eigenfrequencies for the nine A_1 modes calculated in this work.

IR		Raman		Mode assignment
$\mathbf{E}^{\omega} \parallel c$		$y(zz)\bar{y}$		$A_1(i)$
85 K	5 K	85 K	5 K	$i = 1, \ldots, 9$ (calc.)
204	204	-	-	203
261	262	252	252	256
371	370	369	369	371
-	-	442	442	439
456	456	454	454	449
546	547	544	544	549
639	640	637	637	630
717	718	717	717	708
780	781	781	781	775
-	-	668	668	$A_1(7)$(LO)
844	842	841	841	not identified

We tentatively assign the former as the longitudinal optical eigenfrequency of $A_1(7)$ in comparison to a similar observation in $Fe_2Mo_3O_8$ [25], where this mode exhibits similar behavior with almost exactly the same transverse and longitudinal eigenfrequencies. The possible origin of the appearance of longitudinal modes in the Raman spectrum is discussed in detail in Ref. [25]. The origin of the mode at 844 cm^{-1} remains unclear, but a mode with similar eigenfrequency has been observed in $Fe_2Mo_3O_8$ [31,42] suggesting an intrinsic process.

The 12 expected E_1 modes for light polarization $\mathbf{E}^{\omega} \parallel a$ and the Raman configuration $y(xz)\bar{y}$ have been identified in a similar fashion by comparison of our calculated values to reported IR- and Raman modes and are listed in Table VI. The agreement is equally good as for the other channels, but mode $E_1(12)$ at 729 cm^{-1} was only observed in the IR channel. The additional mode which appears only in the Raman channel is tentatively assigned to the longitudinal optical eigenfrequency belonging to $A_1(9)$, following the same arguments as above for the Raman configuration $y(zz)\bar{y}$.

TABLE VI. Experimental excitation frequencies (in cm^{-1}) in $Mn_2Mo_3O_8$ of IR-active modes for light polarization $\mathbf{E}^{\omega} \parallel a$ and Raman-active modes in the Raman configuration $y(xz)\bar{y}$ measured at 85 and 5 K as reported in [31] in comparison to the eigenfrequencies for the 12 E_1 modes calculated in this work.

IR		Raman		Mode
$E^{\omega} \parallel a$		$y(xz)\bar{y}$		assignment
85 K	5 K	85 K	5 K	E_1(i) $i = 1, \ldots, 12$ (calc.)
161	161	159	159	157
188	188	187	186	186
221	221	219	219	216
274	274	272	272	270
307	308	306	307	301
340	341	339	339	337
443	443	442	442	425
460	460	459	459	447
475	476	475	475	464
514	513	513	513	505
562	561	560	560	557
729	729	-	-	721
-	-	781	781	$A_1(9)$(TO)

TABLE VII. Character table of the crystallographic point groups $\mathbf{G} = 6mm$ and the halving subgroup $\mathbf{H} = 6$.

6mm	E	C_6^+	C_6^-	C_3^+	C_3^-	C_2	$3\sigma_d$	$3\sigma_v$
A_1	1	1	1	1	1	1	1	1
A_2	1	1	1	1	1	1	−1	−1
B_1	1	−1	1	1	1	−1	1	−1
B_2	1	−1	1	1	1	−1	−1	1
E_1	2	1	1	−1	−1	−2	0	0
E_2	2	−1	−1	−1	−1	2	0	0
6 (C_6)	E	C_6^+	C_6^-	C_3^+	C_3^-	C_2		
A	1	1	1	1	1	1		
B	1	−1	−1	1	1	−1		
$^1E_1$	1	$-e^{i2\pi/3}$	$-e^{-i2\pi/3}$	$e^{-i2\pi/3}$	$e^{i2\pi/3}$	−1		
$^2E_1$	1	$-e^{-i2\pi/3}$	$-e^{i2\pi/3}$	$e^{i2\pi/3}$	$e^{-i2\pi/3}$	−1		
$^1E_2$	1	$e^{i2\pi/3}$	$e^{-i2\pi/3}$	$e^{-i2\pi/3}$	$e^{i2\pi/3}$	1		
$^2E_2$	1	$e^{-i2\pi/3}$	$e^{i2\pi/3}$	$e^{i2\pi/3}$	$e^{-i2\pi/3}$	1		

APPENDIX B: IRREDUCIBLE COREPRESENTATIONS OF THE MAGNETIC POINT GROUP $6m'm'$

In Table VII we provide the character tables for the point groups $\mathbf{G} = 6mm$ and the halving unitary subgroup $\mathbf{H} = 6$, which constitutes the unitary subgroup of the magnetic point group $\mathbf{M} = 6m'm'$. Following the procedure as described by Anastassakis and Burstein [26], we reduce the irreducible representations of $\mathbf{G} = 6mm$ with respect to the irreducible representations of $\mathbf{H} = 6$ and obtain $A_1, A_2 \to A$, $B_1, B_2 \to B$, $E_1 \to {}^1E_1 + {}^2E_1$, and $E_2 \to {}^1E_2 + {}^2E_2$ as listed in Table VIII. As all irreducible representations of $\mathbf{H} = 6$ are one dimensional, the corepresentations are immediately obtained as given in the last column of Table VIII.

TABLE VIII. Reduction of the irreducible representations of the crystallographic point group $\mathbf{G} = 6mm$ with respect to the unitary halving subgroup $\mathbf{H} = 6$ to determine the corepresentations of the magnetic point group $\mathbf{M} = 6m'm'$.

$\mathbf{g} = \mathbf{G} \oplus \{E + \tau\}$	$\mathbf{G}$ $6mm$	$\mathbf{H}$ 6	$\mathbf{M} = \mathbf{H} + \tau(\mathbf{G} - \mathbf{H})$ $6m'm'$
DA_1	A_1	A	DA
DA_2	A_2	A	DA
DB_1	B_1	B	DB
DB_2	B_2	B	DB
DE_1	E_1	$^1E_1, ^2E_1$	D^1E_1, D^2E_1
DE_2	E_2	$^1E_2, ^2E_2$	D^1E_2, D^2E_2

TABLE IX. Raman tensors of the irreducible (co-) representations for $\mathbf{G} = 6mm$ and $\mathbf{M} = 6m'm'$ in a linear polarization basis [39,47]. Note that in [39] the nomenclature for $D^{1,2}E_1$ and $D^{1,2}E_2$ is interchanged with respect to ours.

$\boldsymbol{A_1}$: $\begin{bmatrix} a & 0 & 0 \\ 0 & a & 0 \\ 0 & 0 & b \end{bmatrix}$	$\boldsymbol{DA}$: $\begin{bmatrix} A & iB & 0 \\ -iB & A & 0 \\ 0 & 0 & I \end{bmatrix}$
$\boldsymbol{A_2}$: $\begin{bmatrix} 0 & c & 0 \\ -c & 0 & 0 \\ 0 & 0 & 0 \end{bmatrix}$	
E_1: $\begin{bmatrix} 0 & 0 & 0 \\ 0 & 0 & d \\ 0 & e & 0 \end{bmatrix}, \begin{bmatrix} 0 & 0 & -d \\ 0 & 0 & 0 \\ -e & 0 & 0 \end{bmatrix}$	$\boldsymbol{D^1E_1, D^2E_1}$: $\begin{bmatrix} 0 & 0 & iC \\ 0 & 0 & C \\ iG & G & 0 \end{bmatrix}, \begin{bmatrix} 0 & 0 & -iF \\ 0 & 0 & F \\ -iH & H & 0 \end{bmatrix}$
E_2: $\begin{bmatrix} 0 & f & 0 \\ f & 0 & 0 \\ 0 & 0 & 0 \end{bmatrix}, \begin{bmatrix} f & 0 & 0 \\ 0 & -f & 0 \\ 0 & 0 & 0 \end{bmatrix}$	$\boldsymbol{D^1E_2, D^2E_2}$: $\begin{bmatrix} D & iD & 0 \\ iD & -D & 0 \\ 0 & 0 & 0 \end{bmatrix}, \begin{bmatrix} E & -iE & 0 \\ -iE & -E & 0 \\ 0 & 0 & 0 \end{bmatrix}$

The reduced Raman tensors for calculating the scattering cross section $I_R \propto |\mathbf{e}_{\mathrm{Sc}}^* \cdot \hat{R} \cdot \mathbf{e}_{\mathrm{In}}|^2$ are given in a linear polarization basis in Table IX for the irreducible representations of $6mm$ [47] and the corepresentations of $6m'm'$ [39]. These symmetry adapted tensors have been tabulated to obtain the corresponding symmetry-adapted functions of the irreducible (co)representation given in Table I. Note that A_2 and the DA modes can have a finite cross section originating from the antisymmetric part of their Raman tensors. These contributions are commonly assumed to be negligible, because the leading order effects should stem from the symmetric parts [57]. Hence, A_2 modes are usually considered as silent modes and treated as if they were forbidden by symmetry.

Using $\mathbf{e}_{\mathrm{Sc,In}} = (x_{\mathrm{s,i}}, y_{\mathrm{s,i}}, z_{\mathrm{s,i}})$, we obtain in the case of A_1

$$\mathbf{e}_{\mathrm{Sc}}^* \begin{bmatrix} a & 0 & 0 \\ 0 & a & 0 \\ 0 & 0 & b \end{bmatrix} \mathbf{e}_{\mathrm{In}} = a(x_{\mathrm{s}}^* x_{\mathrm{i}} + y_{\mathrm{s}}^* y_{\mathrm{i}}) + b z_{\mathrm{s}}^* z_{\mathrm{i}}. \tag{B1}$$

Hence, the A_1 modes should be active in the Raman channels $z(xx)\bar{z}$, $z(yy)\bar{z}$, $x(zz)\bar{x}$, $y(zz)\bar{y}$, but the intensities can be very different for $z(xx)\bar{z}$ and $x(zz)\bar{x}$ due to the different matrix elements a and b. The same holds for the corepresentation DA.

Similarly, the Raman tensor of the irreducible corepresentation $D\,^1E_2$ yields

$$\mathbf{e}_{\mathrm{Sc}}^* \begin{bmatrix} D & iD & 0 \\ iD & -D & 0 \\ 0 & 0 & 0 \end{bmatrix} \mathbf{e}_{\mathrm{In}} = D[x_{\mathrm{s}}^* x_{\mathrm{i}} - y_{\mathrm{s}}^* y_{\mathrm{i}} + i(x_{\mathrm{s}}^* y_{\mathrm{i}} + y_{\mathrm{s}}^* x_{\mathrm{i}})], \tag{B2}$$

in agreement with the characteristic function given in Table I. Similarly, for D^1E_1 we find

$$\mathbf{e}_{\mathrm{Sc}}^* \begin{bmatrix} 0 & 0 & iC \\ 0 & 0 & C \\ iG & G & 0 \end{bmatrix} \mathbf{e}_{\mathrm{In}} = iCx_s^* z_i + Cy_s^* z_i + iGx_i z_s^* + Gy_i z_s^* = Cy_s^* z_i + Gy_i z_s^* + i(Cx_s^* z_i + Gx_i z_s^*), \tag{B3}$$

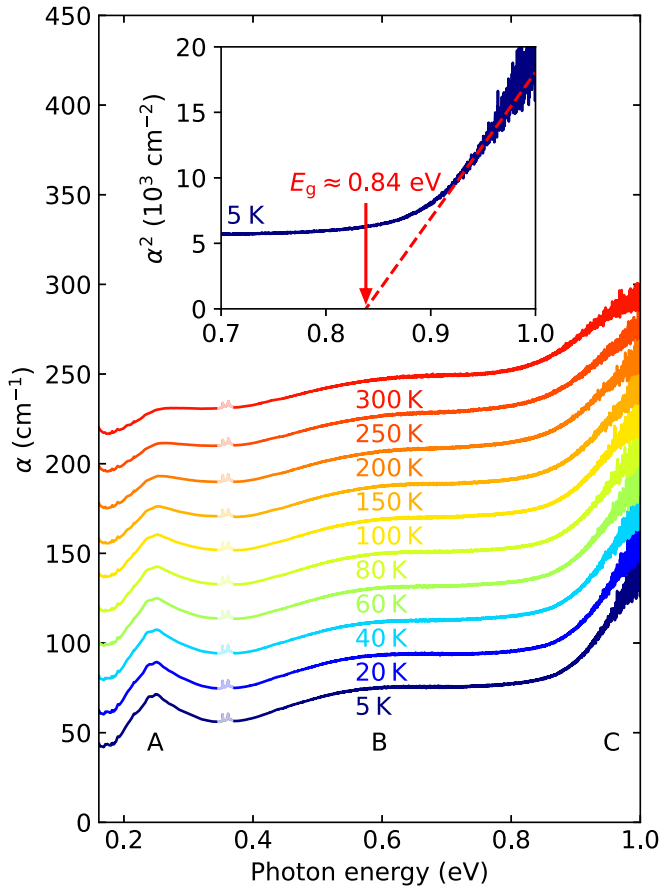


FIG. 6. Temperature-dependent absorption spectra for light polarization $E^{\omega} \parallel a$ in $Mn_2Mo_3O_8$ revealing three excitation bands A, B, C in the MIR/NIR frequency range. In the semitransparent range two narrow lines appear, which are experimental artifacts and not related to $Mn_2Mo_3O_8$. Inset: Plot of α^2 vs energy for the onset of band C at 5 K, yielding an estimate of 0.84 eV for the direct band gap.

which is equivalent to the function in Table I, because the scattering cross section $I_R \propto |\mathbf{e}_{\mathrm{Sc}}^* \cdot \hat{R} \cdot \mathbf{e}_{\mathrm{In}}|^2$ is invariant with respect to any additional phase shift.

APPENDIX C: MIR/NIR ABSORPTION SPECTRA

The assignment of Raman-active longitudinal optical A_1 modes in Table II and Table V was made in analogy to $Co_2Mo_3O_8$, where the occurrence was related to resonant-Raman effects, which can occur, if the frequency of the exciting laser is above the band gap of the materials. Therefore, we performed IR transmission experiments in $Mn_2Mo_3O_8$ to reveal the optical band gap. In Fig. 6, absorption coefficient spectra for light polarization $E^{\omega} \parallel a$ in $Mn_2Mo_3O_8$ are shown in the midinfrared (MIR) and near-infrared (NIR) frequency regime for several temperatures crossing the antiferromagnetic ordering transition at $T_{\mathrm{N}} = 40$ K. The absorption coefficient was determined directly from the transmission coefficient T via $\alpha = -(1/d)\ln T$, where d is the thickness of the sample.

We identify three main broad bands A, B, C, which are visible at all temperatures. Upon cooling the intensity of band A increases and a kind of fine structure becomes visible already

below 150 K, far above magnetic ordering. In contrast, band *B* remains very broad and featureless at all temperatures. We only observe the onset of the highly absorbing band *C* before the sample becomes optically opaque for energies larger than 1 eV. We interpret band *C* as the onset of the semiconducting direct band gap and estimate a gap value of $E_g = 0.84$ eV at 5 K from the plot shown as an inset in Fig. 6. This value is somewhat lower than the value of 1.43 eV estimated from band structure calculations [31].

The origin of bands *A* and *B* is not clear at present, but $Fe_2Mo_3O_8$ and $Co_2Mo_3O_8$ exhibited similar features at slightly different energy ranges [19,25,58], which were attributed to multiplet states for the tetrahedral and octahedral sites of Fe^{2+} and Co^{2+}. Hence, we speculate that this holds true also for the Mn^{2+} states in $Mn_2Mo_3O_8$. Then, the origin of the fine structure of band A may be a signature of vibrationally assisted multiplet states as in many other transition-metal compounds [19,25,58–61].

[1] T. Kurumaji, S. Ishiwata, and Y. Tokura, Doping-tunable ferrimagnetic phase with large linear magnetoelectric effect in a polar magnet $Fe_2Mo_3O_8$, Phys. Rev. X **5**, 031034 (2015).

[2] Y. Wang, G. L. Pascut, B. Gao, T. A. Tyson, K. Haule, V. Kiryukhin, and S.-W. Cheong, Unveiling hidden ferrimagnetism and giant magnetoelectricity in polar magnet $Fe_2Mo_3O_8$, Sci. Rep. **5**, 12268 (2015).

[3] T. Kurumaji, S. Ishiwata, and Y. Tokura, Diagonal magnetoelectric susceptibility and effect of Fe doping in the polar ferrimagnet $Mn_2Mo_3O_8$, Phys. Rev. B **95**, 045142 (2017).

[4] Y. S. Tang, S. M. Wang, L. Lin, C. Li, S. H. Zheng, C. F. Li, J. H. Zhang, Z. B. Yan, X. P. Jiang, and J.-M. Liu, Collinear magnetic structure and multiferroicity in the polar magnet $Co_2Mo_3O_8$, Phys. Rev. B **100**, 134112 (2019).

[5] B. Csizi, S. Reschke, A. Strinić, L. Prodan, V. Tsurkan, I. Kézsmárki, and J. Deisenhofer, Magnetic and vibronic terahertz excitations in Zn-doped $Fe_2Mo_3O_8$, Phys. Rev. B **102**, 174407 (2020).

[6] Y. S. Tang, G. Z. Zhou, L. Lin, R. Chen, J. F. Wang, C. L. Lu, L. Huang, J. H. Zhang, Z. B. Yan, X. M. Lu, X. K. Huang, X. P. Jiang, and J.-M. Liu, Successive electric polarization transitions induced by high magnetic field in the single-crystal antiferromagnet $Co_2Mo_3O_8$, Phys. Rev. B **105**, 064108 (2022).

[7] S. Reschke, D. G. Farkas, A. Strinić, S. Ghara, K. Guratinder, O. Zaharko, L. Prodan, V. Tsurkan, D. Szaller, S. Bordács, J. Deisenhofer, and I. Kézsmárki, Confirming the trilinear form of the optical magnetoelectric effect in the polar honeycomb antiferromagnet $Co_2Mo_3O_8$, npj Quantum Mater. **7**, 1 (2022).

[8] L. Prodan, I. Filippova, A. O. Zubtsovskii, S. Shova, S. Widmann, A. A. Tsirlin, I. Kézsmárki, and V. Tsurkan, Dilution of a polar magnet: Structure and magnetism of Zn-substituted $Co_2Mo_3O_8$, Phys. Rev. B **106**, 174421 (2022).

[9] S. Ghara, E. Barts, K. Vasin, D. Kamenskyi, L. Prodan, V. Tsurkan, I. Kézsmárki, M. Mostovoy, and J. Deisenhofer, Magnetization reversal through an antiferromagnetic state, Nat. Commun. **14**, 5174 (2023).

[10] D. Szaller, L. Prodan, K. Geirhos, V. Felea, Y. Skourski, D. Gorbunov, T. Förster, T. Helm, T. Nomura, A. Miyata, S. Zherlitsyn, J. Wosnitza, A. A. Tsirlin, V. Tsurkan, and I. Kézsmárki, Coexistence of antiferromagnetism and ferrimagnetism in adjacent honeycomb layers, Phys. Rev. B **111**, 184404 (2025).

[11] F. Varret, H. Czeskleba, F. Hartmann-Boutron, and P. Imbert, Étude par effet Mössbauer de l'ion Fe2+ en symétrie trigonale dans les composés du type (Fe, M)2Mo3O8 (M = Mg, Zn, Mn, Co, Ni) et propriétés magnétiques de (Fe, Zn) 2Mo3O8, J. Phys. France **33**, 549 (1972).

[12] F. A. Cotton, Metal atom clusters in oxide systems, Inorg. Chem. **3**, 1217 (1964).

[13] D. Szaller, K. Szász, S. Bordács, J. Viirok, T. Rõõm, U. Nagel, A. Shuvaev, L. Weymann, A. Pimenov, A. A. Tsirlin, A. Jesche, L. Prodan, V. Tsurkan, and I. Kézsmárki, Magnetic anisotropy and exchange paths for octahedrally and tetrahedrally coordinated Mn^{2+} ions in the honeycomb multiferroic $Mn_2Mo_3O_8$, Phys. Rev. B **102**, 144410 (2020).

[14] J. Liao, Z. Huang, B. Zhang, Y. Shangguan, S. Cheng, H. Xu, Z. Song, S. Dong, D. Adrojia, S. Bao, and J. Wen, Magnetic interactions in the polar ferrimagnet $Mn_2Mo_3O_8$ with a bipartite structure, Phys. Rev. B **111**, 024407 (2025).

[15] S. P. McAlister and P. Strobel, Magnetic order in $M_2Mo_3O_8$ single crystals ($M = Mn, Fe, Co, Ni$), J. Magn. Magn. Mater. **30**, 340 (1983).

[16] T. Kurumaji, Y. Takahashi, J. Fujioka, R. Masuda, H. Shishikura, S. Ishiwata, and Y. Tokura, Electromagnon resonance in a collinear spin state of the polar antiferromagnet $Fe_2Mo_3O_8$, Phys. Rev. B **95**, 020405(R) (2017).

[17] F. Wu, S. Bao, J. Zhou, Y. Wang, J. Sun, J. Wen, Y. Wan, and Q. Zhang, Fluctuation-enhanced phonon magnetic moments in a polar antiferromagnet, Nat. Phys. **19**, 1868 (2023).

[18] S. Bao, Z.-L. Gu, Y. Shangguan, Z. Huang, J. Liao, X. Zhao, B. Zhang, Z.-Y. Dong, W. Wang, R. Kajimoto, M. Nakamura, T. Fennell, S.-L. Yu, J.-X. Li, and J. Wen, Direct observation of topological magnon polarons in a multiferroic material, Nat. Commun. **14**, 6093 (2023).

[19] K. V. Vasin, A. Strinić, F. Schilberth, S. Reschke, L. Prodan, V. Tsurkan, A. R. Nurmukhametov, M. V. Eremin, I. Kézsmárki, and J. Deisenhofer, Optical magnetoelectric effect in the polar honeycomb antiferromagnet $Fe_2Mo_3O_8$, Phys. Rev. B **110**, 054401 (2024).

[20] S.-W. Cheong and F.-T. Huang, Altermagnetism with noncollinear spins, npj Quantum Mater. **9**, 13 (2024).

[21] X. Chen, Y. Liu, P. Liu, Y. Yu, J. Ren, J. Li, A. Zhang, and Q. Liu, Unconventional magnons in collinear magnets dictated by spin space groups, Nature (London) **640**, 349 (2025).

[22] S.-W. Cheong and F.-T. Huang, Altermagnetism classification, npj Quantum Mater. **10**, 38 (2025).

[23] L. Šmejkal, J. Sinova, and T. Jungwirth, Beyond conventional ferromagnetism and antiferromagnetism: A phase with nonrelativistic spin and crystal rotation symmetry, Phys. Rev. X **12**, 031042 (2022).

[24] P. A. McClarty, A. Gukasov, and J. G. Rau, Observing altermagnetism using polarized neutrons, Phys. Rev. B **111**, L060405 (2025).

[25] F. Schilberth, M. Kondákor, D. Ukolov, A. Pawbake, K. Vasin, O. Ercem, L. Prodan, V. Tsurkan, A. A. Tsirlin, C. Faugeras, P. Lemmens, K. Penc, I. Kézsmárki, S. Bordács, and J. Deisenhofer, Optical phonons as a testing ground for spin group symmetries, npj Quantum Mater. **11**, 26 (2026).

[26] E. Anastassakis and E. Burstein, Morphic effects. V. Time reversal symmetry and the mode properties of long wavelength optical phonons, J. Phys. C **5**, 2468 (1972).

[27] E. Anastassakis and E. Burstein, Morphic effects I-effects of external forces on photon-optical phonon interactions, J. Phys. Chem. Solids **32**, 313 (1971).

[28] E. Anastassakis and E. Burstein, Morphic effects II-effects of external forces on the frequencies of the $q \approx 0$ optical phonons, J. Phys. Chem. Solids **32**, 563 (1971).

[29] E. Anastassakis, E. Burstein, A. Maradudin, and R. Minnick, Morphic effects — III. Effects of an external magnetic field on the long wavelength optical phonons, J. Phys. Chem. Solids **33**, 519 (1972).

[30] E. Anastassakis, E. Burstein, A. Maradudin, and R. Minnick, Morphic effects-IV. Effects of an applied magnetic field on first-order photonoptical phonon interactions in non-magnetic crystals, J. Phys. Chem. Solids **33**, 1091 (1972).

[31] T. N. Stanislavchuk, G. L. Pascut, A. P. Litvinchuk, Z. Liu, S. Choi, M. J. Gutmann, B. Gao, K. Haule, V. Kiryukhin, S.-W. Cheong, and A. A. Sirenko, Spectroscopic and first principle DFT+eDMFT study of complex structural, electronic, and vibrational properties of $M_2Mo_3O_8$ (M = Fe, Mn) polar magnets, Phys. Rev. B **102**, 115139 (2020).

[32] T. N. Stanislavchuk, T. D. Kang, P. D. Rogers, E. C. Standard, R. Basistyy, A. M. Kotelyanskii, G. Nita, T. Zhou, G. L. Carr, M. Kotelyanskii, and A. A. Sirenko, Synchrotron radiation-based far-infrared spectroscopic ellipsometer with full Mueller-matrix capability, Rev. Sci. Instrum. **84**, 023901 (2013).

[33] A. Messiah, *Quantum Mechanics, volume II* (Amsterdam: North-Holland Publishing Company, Amsterdam, 1961).

[34] M. Born, E. Wolf, A. B. Bhatia, P. C. Clemmow, D. Gabor, A. R. Stokes, A. M. Taylor, P. A. Wayman, and W. L. Wilcock, *Principles of Optics: Electromagnetic Theory of Propagation, Interference and Diffraction of Light* (Cambridge University Press, Cambridge, 1999).

[35] G. Kresse and J. Furthmüller, Efficiency of *ab-initio* total energy calculations for metals and semiconductors using a plane-wave basis set, Comput. Mater. Sci. **6**, 15 (1996).

[36] G. Kresse and J. Furthmüller, Efficient iterative schemes for *ab initio* total-energy calculations using a plane-wave basis set, Phys. Rev. B **54**, 11169 (1996).

[37] J. P. Perdew, K. Burke, and M. Ernzerhof, Generalized gradient approximation made simple, Phys. Rev. Lett. **77**, 3865 (1996).

[38] C. J. Bradley and A. P. Cracknell, *The Mathematical Theory of Symmetry in Solids: Representation Theory for Point Groups and Space Groups* (Oxford University Press, Oxford, 2009).

[39] A. P. Cracknell, Scattering matrices for the Raman effect in magnetic crystals, J. Phys. C **2**, 500 (1969).

[40] T. C. Damen, S. P. S. Porto, and B. Tell, Raman effect in zinc oxide, Phys. Rev. **142**, 570 (1966).

[41] D. L. Rousseau, R. P. Bauman, and S. P. S. Porto, Normal mode determination in crystals, J. Raman Spectrosc. **10**, 253 (1981).

[42] S. Reschke, A. A. Tsirlin, N. Khan, L. Prodan, V. Tsurkan, I. Kézsmárki, and J. Deisenhofer, Structure, phonons, and orbital degrees of freedom in $Fe_2Mo_3O_8$, Phys. Rev. B **102**, 094307 (2020).

[43] D. Bertrand and H. Kerner-Czeskleba, Étude structurale et magnétique de molybdates d'éléments de transition, J. Phys. France **36**, 379 (1975).

[44] H. Schiff, A. Corticelli, A. Guerreiro, J. Romhányi, and P. A. McClarty, The crystallographic spin point groups and their representations, SciPost Phys. **18**, 109 (2025).

[45] Y. Tatsumi, T. Kaneko, and R. Saito, Conservation law of angular momentum in helicity-dependent Raman and Rayleigh scattering, Phys. Rev. B **97**, 195444 (2018).

[46] L. Zhang and Q. Niu, Angular momentum of phonons and the Einstein–de Haas effect, Phys. Rev. Lett. **112**, 085503 (2014).

[47] W. Hayes and R. Loudon, *Scattering of Light by Crystals* (Dover Publications, Mineola, New York, 2004).

[48] Martin and Falicov, *Light Scattering in Solids I*, edited by M. Cardona (Springer, Berlin, Heidelberg, 1983).

[49] J. B. Sokoloff, Microscopic theory of modifications of first order Raman scattering caused by magnetic ordering, J. Phys. C **5**, 2482 (1972).

[50] Y. Tanabe, T. Moriya, and S. Sugano, Magnon-induced electric dipole transition moment, Phys. Rev. Lett. **15**, 1023 (1965).

[51] Y. Tanaka and K. Nagasaka, Far infrared activity due to two-magnon excitation in antiferromagnetic $MEM(TCNQ)_2$, Solid State Commun. **73**, 735 (1990).

[52] Y. Tanabe, Y. Fujimaki, K. Kojima, S. Uchida, S. Onari, T. Matsuo, S. Azuma, and E. Hanamura, Direct optical excitation of two and three magnons in α-Fe_2O_3, Low Temp. Phys. **31**, 780 (2005).

[53] L. Peedu, V. Kocsis, D. Szaller, B. Forrai, S. Bordács, I. Kézsmárki, J. Viirok, U. Nagel, B. Bernáth, D. L. Kamenskyi, A. Miyata, O. Portugall, Y. Tokunaga, Y. Tokura, Y. Taguchi, and T. Rõõm, Terahertz spectroscopy of spin excitations in magnetoelectric $LiFePO_4$ in high magnetic fields, Phys. Rev. B **106**, 134413 (2022).

[54] J. W. Halley and I. Silvera, Odd-exciton magnon interaction and explanation of anomalous far-infrared absorption in antiferromagnetic FeF_2, Phys. Rev. Lett. **15**, 654 (1965).

[55] S. J. Allen, R. Loudon, and P. L. Richards, Two-magnon absorption in antiferromagnetic MnF_2, Phys. Rev. Lett. **16**, 463 (1966).

[56] F. Schilberth, K. Vasin, M. Knauft, M. Kondkor, M. Vuckovic, N. Herrmann, K. Penc, M. Minola, B. Keimer, V. A. Martinez, K. Panda, A. Sirenko, L. Prodan, V. Tsurkan, A. A. Tsirlin, I. Kézsmárki, and J. Desienhofer, Raman and THz spectra for the publication: Magnetic circular dichroism of THz modes and selection rules of Raman-active optical phonons in the polar altermagnet candidate $Mn_2Mo_3O_8$ [Dataset], Zenodo, 2026, doi:10.5281/zenodo.22803844.

[57] J. Birman, *Licht und Materie Ib / Light and Matter Ib*, Handbuch der Physik Encyclopedia of Physics (Springer, Berlin, Heidelberg, 1974).

[58] K. Park, G. L. Pascut, G. Khanal, M. O. Yokosuk, X. Xu, B. Gao, M. J. Gutmann, A. P. Litvinchuk, V. Kiryukhin, S. W. Cheong, D. Vanderbilt, K. Haule, and J. L. Musfeldt, Band-Mott

mixing hybridizes the gap in $Fe_2Mo_3O_8$, Phys. Rev. B **104**, 195143 (2021).

[59] J. Deisenhofer, I. Leonov, M. V. Eremin, C. Kant, P. Ghigna, F. Mayr, V. V. Iglamov, V. I. Anisimov, and D. van der Marel, Optical evidence for symmetry changes above the Néel temperature of $KCuF_3$, Phys. Rev. Lett. **101**, 157406 (2008).

[60] M. Schmidt, Z. Wang, C. Kant, F. Mayr, S. Toth, A. T. M. N. Islam, B. Lake, V. Tsurkan, A. Loidl, and J. Deisenhofer, Exciton-magnon transitions in the frustrated chromium antiferromagnets $CuCrO_2$, α-$CaCr_2O_4$, $CdCr_2O_4$, and $ZnCr_2O_4$, Phys. Rev. B **87**, 224424 (2013).

[61] V. Kocsis, S. Bordács, J. Deisenhofer, L. F. Kiss, K. Ohgushi, Y. Kaneko, Y. Tokura, and I. Kézsmárki, Strong magneto-optical effects in ACr_2S_4 (A = F, Co) spinel oxides generated by tetrahedrally coordinated transition metal ions, Phys. Rev. B **97**, 125140 (2018).